Modeling the stimulatory network in Natural Killer cells

Sahak Z. Makaryan[1] and Stacey D. Finley[2]

[1]Department of Biomedical Engineering, University of Southern California, Los Angeles, CA, USA

[2]Department of Biomedical Engineering; Mork Family Department of Chemical Engineering and Materials Science; Department of Biological Sciences, University of Southern California, Los Angeles, CA, USA

ABSTRACT

Natural killer (NK) cells are innate immune cells that eliminate diseased cells by releasing cytotoxic chemicals upon activation. Excitingly, NK cell-based immunotherapies are shown to be effective against hematological cancers; however, similar success against solid tumors still remains a challenge. A better understanding of the pathways regulating NK cell activation can provide insight into strategies for optimizing these therapies. We constructed a mechanistic model of the CD16, 2B4 and NKG2D stimulatory pathways. The model was fit to published data and validated with a separate dataset. Baseline model predictions demonstrate the qualitative similarities between CD16 and NKG2D stimulation; they activate the downstream species to a greater degree and at a faster rate when compared to 2B4. Contrastingly, 2B4 stimulation activates the signaling species over a longer time interval. Interestingly, the model predicts that 2B4 co-stimulation with either CD16 or NKG2D produces optimum activation of the Src family kinases (SFK), which are the species responsible for initiating signal transduction. *In silico* perturbations of the signaling networks highlight how phosphatases control signal transduction. Moreover, inhibiting the activation of the phosphatases is predicted to significantly enhance species activation. In summary, the model predicts: (1) qualitative differences between the pathways, (2) co-stimulation of qualitatively different pathways induces optimal activation of the signal transducer (pSFK) and (3) inhibiting the activation of the inhibitor significantly increases the rate and magnitude of species activation. This detailed mechanistic insight can help design NK cell-based immunotherapies.

1 INTRODUCTION

A few areas of biology provide new opportunities to be explored by quantitative, engineering-based computational models (1). In particular, tumor immunology can benefit from robust computational modeling. Recently, the advent of cancer immunotherapy (2,3) has engendered a new hope for cancer patients. In fact, immunotherapy is considered a breakthrough therapeutic approach in the clinic, especially as an effective treatment for hematological cancers (4–6). Ongoing work is aimed at achieving similar success for solid tumors, and computational modeling can aid in these efforts.

Natural killer (NK) cells are immune cells that interact with solid tumors (7–9). NK cells express a repertoire of stimulatory receptors that mediate the release of cytotoxic chemicals upon cell contact. This, in turn, induces cell death of the target cells. Previously, researchers have studied NK cell activation under different conditions using mathematical models. For example, work by Das demonstrates how receptor-ligand interactions impact NK cell activation using phosphorylated Erk (pErk) as a readout (10). Mesecke and colleagues determined that the physical association of Src family kinases (SFK) with a stimulatory receptor is essential for NK cells to promote a cytotoxic response (11). In both cases, the mathematical models simulate an individual stimulatory receptor, which does not account for the fact that NK cells express several different stimulatory receptors that contribute to cell activation. An analysis of multiple stimulatory receptors is necessary for determining which pathways, and in which combinations, best activate the stimulatory network. In fact, there is currently no quantitative study that: (1) compares the effects of different stimulatory pathways on NK cell stimulation, (2) demonstrates how different combinations of receptor co-stimulation activates the signaling species and (3) predicts how the stimulatory network can be perturbed such that species activation is enhanced. Such a computational study can provide insight for optimizing NK cell-based immunotherapies. Here, we present a new computational model that goes beyond previous models (10–16) by including more molecular detail and by addressing the aforementioned knowledge gaps.

The CD16, 2B4 and NKG2D stimulatory pathways were modeled in this study. These pathways differ in the context of NK cell activation (17–19). CD16 is an Fc receptor that binds to the constant region of antibodies. This emphasizes CD16's activation in antibody-dependent cell-mediated cytotoxicity (ADCC). Its cytoplasmic domain is associated with CD3ζ, which contains immunoreceptor tyrosine-based activation motifs (ITAM). 2B4 is part of the signaling lymphocytic activation molecule (SLAM) family of receptors, and its cytoplasmic tail contains four immunoreceptor tyrosine-based switch motifs (ITSM). The ligand for 2B4, CD48, is expressed by cells of hematopoietic origin. This suggests 2B4 may play a role in regulating hematopoietic processes. NKG2D belongs to the family of C-type lectin-like receptors. It associates with the adaptor protein DAP10, which has an activation motif that is similar to the CD28 T cell co-receptor. NKG2D binds to ligands typically expressed by cells that have undergone transformation, which implicates this receptor in the elimination of tumors.

Ligand binding to the CD16, 2B4 and NKG2D receptors initiates intracellular signaling through multiple pathways. The PI3K-Akt, SLP76-Vav-Erk and PLCγ networks are all activated upon CD16, 2B4 and NKG2D stimulation (20). In NK cell biology, the PI3K-Akt pathway promotes cell survival, while Erk activation is correlated with cell proliferation. SLP76 and Vav activation are necessary for actin remodel-

ing and the formation of the immunological synapse. Lastly, PLCγ activation induces the release of intracellular calcium ions, which subsequently activates the cell. The integration of these intracellular signaling reactions is necessary to activate NK cells. Many of the downstream reactions are common between the pathways with only subtle differences. Specifically, 2B4 leads to PI3K activation, but does not induce Akt phosphorylation (21,22). Additionally, 2B4 and NKG2D specifically lead to phosphorylation of the Y113 and Y128 sites on SLP76, respectively, while CD16 induces activation of both sites (21). Also, CD16 induces ZAP70 and LAT activation, while 2B4 and NKG2D do not.

In the present study, we use mathematical modeling to characterize and compare the signaling dynamics of the individual stimulatory pathways with respect to their magnitude and kinetics of activation of the network. Furthermore, the effects of receptor co-stimulation are explored, which helps identify which combination optimally activates the stimulatory network. *In silico* perturbations of the stimulatory network reveal which species serve as gate-keepers of cell stimulation and how changing their activation rates affects signal transduction. In total, the model provides a theoretical framework for NK cell stimulation, and the predictions can be used for optimizing NK cell-based therapies.

2 METHODS

Model construction. The model was constructed using Michaelis-Menten reactions in BioNetGen (23) and was simulated in MATLAB (MathWorks). The model contains 138 rate constants and 42 species, including the three receptors. Each receptor binds to its ligand and forms a receptor-ligand complex that allows the receptor to become phosphorylated by basally active Src family kinases (SFK). Then, the ligand-bound phosphorylated receptor serves as the catalyst for activating SFK from a basally the active state to a fully active state (pSFK).

Fully active SFK mediates the phosphorylation (activation) of a number of downstream signaling species, including LAT, ZAP70, PI3K, PLCγ, Vav and SLP76. Phosphorylated ZAP70 also promotes activation of LAT. Phosphorylated PLCγ promotes the release of intracellular calcium ions (10,11,21,22,24). Phosphorylated PI3K promotes the phosphorylation of PIP_2 to form PIP_3. The inhibitory species, phosphatases SHP and SHIP, in our NK cell activation model serves to provide negative feedback onto the system (25).

Two important downstream species included in the model are Erk and Akt. The catalyst for Akt phosphorylation is PIP_3. The catalysts for Erk phosphorylation are the phosphorylated forms of SLP76, as well as the phosphorylated form of Vav. These species are upstream components to the MAPK pathway (10,11).

The initial concentrations of the species in our system were extracted from scientific literature (26–29). We simulate the dynamics of the signaling network for 30 minutes, to focus on the initial stimulus. Given this time scale, we assume that the synthesis of species is negligible compared to phosphorylation and dephosphorylation reactions (10,11). Lastly, we included a non-specific degradation reaction of the phosphorylated species in the system to account for degradation, dilution and disappearance of the active species, as observed in experimental measurements (21,24,30–32).

Data collection and processing. To control for variations in the experimental conditions, we only used data from published studies where (1) the antibodies used for CD16, 2B4 and NKG2D stimulation were of the same concentration (10 μg/mL) and from the same vendor, and (2) the cell types used in these studies were primary NK cells. Immunoblot images from these published studies were analyzed and processed using ImageJ. Specifically, ImageJ provides a measure of the optical density for any pre-defined rectangular space of an image in gray-scale that ranges in value from 0 – 225 (black to white, respectively). Protein bands in Western blots were analyzed to estimate their density. To control for immunoblot variations across the experiments, we subtracted the optical density measurement of the Western blot gel background from the optical density measurements of all protein bands in the same gel. Furthermore, for a single protein, the optical density measurement of the zeroth time point was also subtracted from the optical density measurements of the remaining time points. This procedure, which is provided by ImageJ's usage protocol, standardizes the experiments for comparison and controls for the background and zeroth time point measurements. In total, the model was trained to 60 data points across ten different species, with a minimum of three data points for a single species. Additionally, the model was validated against 43 data points. The signal intensity $\left(Q_{pX_j}\right)$ of a given phosphorylated species (pX) at the jth time point is calculated as:

$$Q_{pX_j} = \frac{OD_{pX_j}}{OD_{Control_j}}$$

where OD_{pX_j} and $OD_{Control_j}$ are the optical density values of the phosphorylated species and a loading control, respectively, at the jth time point. Furthermore, the signal intensity $\left(Q_{pX}\right)$ was normalized to a single (reference) time point $\left(Q_{pX_{ref}}\right)$ by calculating the percent change $\left(\%\Delta_{pX}\right)$ as follows:

$$\%\Delta_{pX_j} = \frac{Q_{pX_j} - Q_{pX_{ref}}}{Q_{pX_{ref}}} \times 100\%$$

Sensitivity analysis. The extended Fourier Amplitude Sensitivity Test (eFAST) was used to calculate the sensitivity of the model outputs to its inputs (33) . The outputs of the analysis are the reaction rates, and the rate constants and initial concentrations are the inputs. Briefly, eFAST is a variance-based sensitivity analysis that uses a variance decomposition method similar to ANOVA. The variance of an output is partitioned, and the algorithm determines what fraction of the variance in an output can be explained by the variation in each input. The greater the output's variance is attributed to an input, the greater the input's influence is on the output. The first-order sensitivity index, S_i, measures the fraction of the model output's variance explained by the ith parameter's input variance:

$$S_i = \frac{\sigma_i^2}{\sigma_{total}^2}$$

To estimate the total-order sensitivity index, S_{Ti}, of a given parameter i, eFAST calculates the summed sensitivity index of the complementary set of parameters (i.e. all parameters except i). S_{Ti} is then calculated as the remaining variance excluding the contribution of the complementary set, S_{Ci}, as follows:

$$S_{Ti} = 1 - S_{Ci}$$

Thus, the S_{Ti} for a given input I measures how influential that input and all of its interactions with other parameters are to a specific output. We selected to fit parameters with an $S_{Ti} \geq 0.5$ for all the model outputs. If both k_{on} and k_{off} for a single reaction were estimated to have an $S_{Ti} \geq \pm 0.5$, then k_{on} was kept constant at 10^{-1} $\mu M^{-1}s^{-1}$, as the association rate constant is reported to be fairly consistent across bimolecular reactions (26,27). We implemented the eFAST analysis based on the algorithm outlined by Marino and coworkers (33). For sensitivity analysis, we varied the inputs ±10-fold from baseline values.

Parameter estimation. The values of the parameters shown to be influential based on the sensitivity analysis were estimated using Particle Swarm Optimization (PSO) (34). This computational method estimates the parameter values by minimizing an objective function (J). Here, we included a regularization term in L_2 (i.e., Tikhonov regularization (35)) to prevent over-fitting. The objective function is as follows:

$$J = \|\mathbf{y} - \mathcal{M}(\boldsymbol{\theta})\|_2^2 + \alpha\|\boldsymbol{\theta}\|_2^2$$

where $\mathbf{y}$ is our data vector, $\mathcal{M}(\boldsymbol{\theta})$ is our model prediction vector, which uses the parameter set $\boldsymbol{\theta}$ as its argument and α (set to one in this analysis) is a parameter that balances the amount of emphasis given to minimizing the first term versus the second term in J. The algorithm works by having a population of candidate solutions to explore the defined parameter space. Each candidate solution is guided by its own best-known position in the search-space based on the value of the objective function, as well as the entire set of candidate solutions' best-known positions. When improved positions are found, then these positions will guide the subsequent set of candidate solutions. This process is repeated until a satisfactory solution is discovered (i.e., J is minimized) or a specified maximum number of iterations is reached. Since the starting positions in the parameter space can influence the final result, we executed the algorithm 100 times using randomized initial guesses. The search-space in PSO spanned ±10-fold from baseline value for each estimated parameter. The model's predicted levels of the phosphorylated species were processed in the same way as the experimental data (see above). That is, the reference time point for normalizing the predicted phosphorylated species values was the same time point used to normalize the corresponding experimental data points.

Cluster analysis and principal component analysis. The PSO algorithm estimated the 37 fitted parameters 100 different times. The parameter matrix ($\boldsymbol{\theta}$), therefore, has dimensions $p \times n$ where p is the number of parameters and n is the number of estimated parameter sets. We used the MATLAB function *kmeans*, which employs the *k-means*$^{++}$ clustering algorithm, to identify similar groups in $\boldsymbol{\theta}$, resulting in three distinct clusters. The MATLAB function *pca* was used to identify which estimated parameters best explain the variance in $\boldsymbol{\theta}$.

Parameter probability density estimation.To understand the robustness of the model parameters, we determined the distribution of the optimal parameter values (the probability density function) for each of the estimated parameters in each cluster. Let $\mathbf{C}_i$ denote the partitioned parameter matrix ($\boldsymbol{\theta}$) of the ith cluster. The clusters differ in the number of estimates, with clusters 1, 2 and 3 having 22, 49 and 29 of the initial 100 estimates, respectively. We estimated the probability densities of each of the 37 fitted parameter using bootstrapping and Monte Carlo methods. Briefly, bootstrapping is a method of assessing the distribution of statistical metrics (e.g., mean, variance, etc.). First, hypothetical data sets of the same size as the original data set are generated from the original data by resampling with replacement. These synthetic data sets are defined as bootstrapped samples. Next, the mean and covariance of the parameters of each cluster are calculated for each bootstrapped sample. Then, for each bootstrapped sample, we generate a random vector from a multivariate normal distribution with a mean vector and covariance matrix from the previous step. This process is repeated a large amount of times to construct the distribution of the estimated parameters.

Signaling time. We define the signaling time ($\boldsymbol{\mu}$) as the average amount of time required for a species to become activated. We follow the techniques described previously (36). We first define the function $f(t)$ as the species' concentration over time, then calculate ($\boldsymbol{\mu}$) as:

$$\boldsymbol{\mu} = \frac{\boldsymbol{T}}{\boldsymbol{I}}$$

where $\boldsymbol{T} = \int_0^\infty t f(t) dt$ and $\boldsymbol{I} = \int_0^\infty f(t) dt$. This is analogous to finding the mean value of a statistical distribution.

Signal duration. We define the signal duration ($\boldsymbol{\tau}$) as the average amount of time the species remains activated. We again define the function $f(t)$ as the species' concentration over time, then calculate $\boldsymbol{\tau}$ as:

$$\boldsymbol{\tau} = \sqrt{\frac{\boldsymbol{Q}}{\boldsymbol{I}} - \boldsymbol{\mu}^2}$$

where $Q = \int_0^\infty t^2 f(t) dt$. This is analogous to finding the standard deviation of a distribution.

Signal strength. We define signal strength ($\boldsymbol{\lambda}$) as the average amount activated species where,

$$\boldsymbol{\lambda} = \frac{\boldsymbol{I}}{2\boldsymbol{\tau}}$$

Here, the area under the curve of a species concentration ($\boldsymbol{I}$) is equal to the area of a rectangle whose dimensions are $\boldsymbol{\lambda}$ and $2\boldsymbol{\tau}$.

3 RESULTS AND DISCUSSION

3.1 Model calibration and validation

We generated a mathematical model of NK cell signaling that includes three main pathways: CD16, 2B4 and NKG2D. When these receptors are stimulated, they activate the cell via cascades of phosphorylation reactions (**Figure 1**): activation of the Src family kinases (SFK), facilitated by the ligand-bound phosphorylated receptors, catalyzes the activation of the PI3K-Akt, SLP76-Vav-Erk, and PLCγ pathways. We simulated these reactions in the form of ordinary differential equations (ODEs) using established Michaelis-Menten kinet-

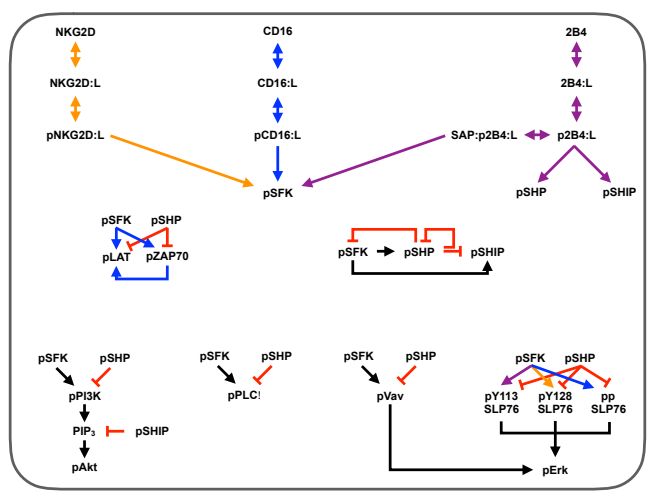

Fig. 1. Model schematic. Reaction network for three stimulatory receptors expressed on the surface of NK cells: CD16, 2B4 and NKG2D. These receptors promote signaling species that mediate NK cell activation: SFK, Erk, Akt and PLCγ. Arrows indicate stimulation, while red crossbars indicate inhibition. Orange arrows are specific to the NKG2D pathway; blue, CD16 pathway; purple, 2B4 pathway; black, all pathways.

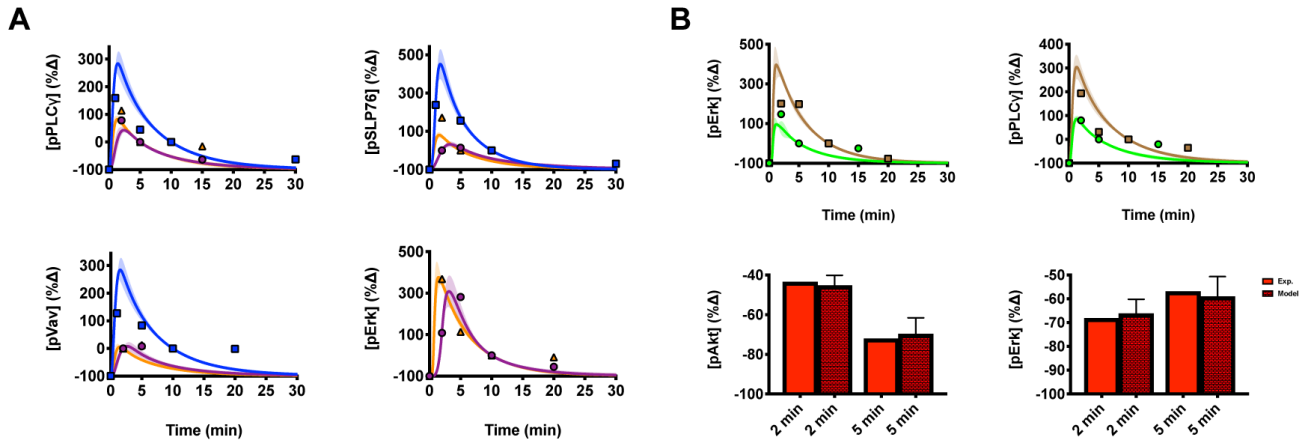

Fig. 2. Model calibration and validation. (**A**) The model was fit to experimental data for pPLCγ (*top left*), pSLP76 (*top right*), pVav (*bottom left*) and pErk (*bottom right*). (**B**) The model predictions were validated against separate data for pErk (*top left*) and pPLCγ (*top right*) under co-stimulation of 2B4 and NKG2D without inhibition. PI3K inhibition (*bottom left*) and MEK inhibition (*bottom right*) were simulated under co-stimulation of 2B4 and NKG2D, and the percent change in pAkt and pErk, respectively, was recorded at different time points. Blue: CD16 pathway. Purple: 2B4 pathway. Orange: NKG2D pathway. Green and Brown: 2B4 and NKG2D pathways from separate experimental studies. Solid lines: mean model predictions. Shaded area: standard deviation of mean model predictions. Squares, circles and triangles: experimental data. Bars: mean value. Error bars: standard deviation of experimental data. Here, we show a subset of the data used for calibration and validation; the additional data are shown in Figure S3.

ics. The model is provided in Supplementary Files S1 and S2. The model was calibrated to immunoblot data (21,24,30,32). We quantified the temporal change in the optical density of protein bands from images of immunoblot experiments using ImageJ (NIH). Specifically, we used the normalized levels of phosphorylated species: pSFK, pZAP70, pLAT, ppSLP76, PLCγ, pVav, pErk, pAkt, and SLP76 phosphorylated at pY113 and pY128.

We estimated the parameter values as follows. We first applied a global sensitivity analysis (33) at different time-points to identify influential parameters in the model by quantifying how much the rate of each reaction (output) varies based upon variations in each parameter (i.e., k_{on}, k_{off}, k_{cat}, and initial concentrations; inputs). The results of this sensitivity analysis identified 37 parameters (Supplementary File S3) that significantly impact the model's reaction rates (**Figure S1**). Next, we estimated the values of these influential parameters using particle swarm optimization (PSO) (34). This algorithm searches the parameter-space for solutions that minimize the error between the model predictions and the experimental data. Here, the objective function was a combination of ordinary least squares (OLS) and a regularization term to prevent over-fitting (see Methods). The algorithm was executed 100 times using random initial guesses, which resulted in 100 estimates for each of the 37 parameters (**Figure S2**). The results from model calibration (**Figure 2A**) show that the model predictions quantitatively match the experimental data for mono-stimulation of CD16 (blue lines), 2B4 (purple lines), and NKG2D (orange lines). More results from model calibration can be found in **Figure S3A**.

To validate the model, we compared the model predictions to separate experimental data. Specifically, we quantified the optical density of intracellular species from immunoblot images when 2B4 and NKG2D were simultaneously stimulated with and without molecular perturbations (e.g., RNA interference, kinase inhibitors, or species knockdown) (24,31,37–39). RNA interference and species knockdown experiments were simulated by decreasing the initial concentration of the species of interest in our model, and kinase inhibitors were simulated by decreasing the reaction rates of interest. The results from model validation are shown in **Figure 2B**. The model captures the co-stimulation of 2B4 and NKG2D without inhibition (**Figure 2B,** *top panel*) and in the presence of various perturbations that inhibit signaling (**Figure 2B,** *bottom panel*). The presence of PI3K inhibitor was simulated by decreasing PI3K activity via 15% (**Figure 2B,** *bottom left panel*). Also, the presence of MEK inhibitor was simulated by decreasing the rate of pErk activation by 55% (**Figure 2B,** *bottom right panel*). Additional results from model validation are shown in **Figure S3B**. Altogether, the model accurately predicts the effects of a variety of perturbations. This validated model allows us to perform simulations and make meaningful comparisons amongst the pathways.

3.2 Cluster analysis and parameter probability density estimation

As the model was fitted to normalized data using 100 independent iterations, it is likely that the 100 parameter sets from PSO could result in different absolute values. Therefore, we used the *k*-means clustering algorithm (40), as well as principal component analysis (PCA) (41), to group the 100 parameter sets (see Methods). We determined the optimal number of clusters using a silhouette (**Figure S4A**) and elbow plot (**Figure S4B**). As a result, we identified three unique clusters (**Figure 3**). Analysis of the principal components reveals that the clusters are mostly separated by the initial concentrations of Erk and SLP76 (PC1 and PC2, respectively), and together explain more than 70% of the variance. Based on these results, we proceeded to analyze the model predictions not only across the three pathways but also across the three clusters.

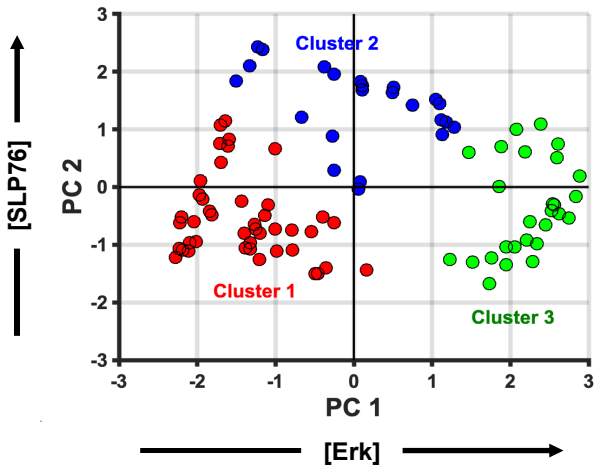

Fig. 3. Groups in the estimated parameters. The *k-means*$^{++}$ clustering algorithm was used to identify groups with similar parameter estimates. Principal component analysis identified the parameters that collectively explain the variance in the original parameter estimates. Increasing from left to right on the-axis corresponds to increasing ERK initial concentration. Increasing from bottom to top on the-axis corresponds to increasing SLP76 initial concentration.

Clusters 1, 2 and 3 contained 22, 49 and 29 of the initial 100 parameter sets, respectively. We quantified the level of uncertainty in our estimation for the 37 parameters within each cluster using bootstrap resampling (42,43) and Monte Carlo methods. A schematic of this process can be found in **Figure S5**. Furthermore, probability density distributions for each parameter were estimated (**Figure S6**).

3.3 Differences and similarities in baseline signaling dynamics

To simulate NK cell activation, we predicted the time courses of the activated species following stimulation of each receptor. We characterized the concentration time courses using the following metrics: signaling time (μ), signaling duration (2τ), and signal strength (λ), as described previously (36) (see Methods). Signaling time is defined as the average amount of time required for species activation. Signal duration is the average length of time the species is activated. Signal strength is the average amount of activated species. A geometrical interpretation of these metrics can be found in **Figure S7**.

The baseline model was simulated using 66.7 nM of ligand concentration, mimicking the experimental studies (21,24,30,32) used to train the model (**Figure 4**). For each cluster, and for each pathway, 1,000 parameter estimates were used to simulate the signaling dynamics. In **Figure 4**, we show the median result of the 1,000 simulations, along with the 95% confidence interval. The signaling time of pSFK (**Figure 4A**, *left column*) in clusters 1 and 2 is faster under CD16 or NKG2D stimulation (~1 minute faster) when compared to 2B4 stimulation (p<0.05); in cluster 3, however, the differences between the pathways are negligible. The signaling time of pErk (**Figure 4B**, *left column*) is shown to be faster via CD16 or NKG2D (~2 minutes faster) than 2B4 (p<0.05). Similarly, the signaling time of PLCγ (**Figure 4C**, *left column*), pVav (**Figure 4D**, *left column*) and pSLP76 (**Figure 4E**, *left column*) are uniformly faster under CD16 or NKG2D stimulation, compared to 2B4 (p<0.05). The signaling time of pAkt (**Figure 4F** *left column*), however, shows no significant differences across the pathways. Instead, the main differences are between the clusters, where in cluster 3, the signaling time is about 4 and 6 minutes faster when compared to clusters 1 and 2, respectively (p<0.05).

The signal duration of pSFK (**Figure 4A**, *middle column*) in cluster 1 is predicted to be about 30 seconds and 1 minute longer under 2B4 stimulation when compared to NKG2D and CD16 stimulation, respectively (p<0.05)). In clusters 2 and 3, however, the pathway differences in signal duration are negligible. In cluster 1, the signal duration of pErk (**Figure 4B**, *middle column*) is approximately 1 minute longer under 2B4 stimulation compared to CD16 or NKG2D (p<0.05). In clusters 2 and 3, the pathway differences in the signal duration of pErk are comparable. The signal duration of PLCγ **Figure 4C**, *middle column*), pVav (**Figure 4D**, *middle column*) and pSLP76 (**Figure 4E**, *middle column*) are longer under 2B4 stimulation (p <0.05). The signal duration of pAkt (**Figure 4F**, *middle column*) varies only amongst the clusters, where cluster 2 displays a longer signal by 2 and 8 minutes when compared to clusters 1 and 3, respectively (p<0.05).

The signal strength of pSFK (**Figure 4A**, *right column*) is greater under the CD16 and NKG2D pathways, compared to 2B4 stimulation. Here, cluster 3 shows the greatest difference between the three pathways, where pSFK signal strength is approximately 60% and 100% higher with CD16 or NKG2D stimulation compared to 2B4, respectively (p<0.05). The activation of pErk (**Figure 4B**, *right column*), similarly, is greater with CD16 or NKG2D stimulation (p<0.05) when compared to 2B4, and this difference is readily observed in cluster 3, where the initial concentration of Erk is greatest (**Figure S6**). The differences in the signal strength of PLCγ (**Figure 4C**, *right column*) are explained by the clusters, with cluster 1 generating the most PLCγ (p<0.05). Likewise, the differences in the signal strength of pVav (**Figure 4D**, *right column*) are determined by the clusters, with clusters 1 and 3 showing a greater amount of pVav activation than cluster 2 (p<0.05).). In the case of pSLP76's signal strength (**Figure 4E**, *right column*), the model predicts both differences across the pathways and clusters. Specifically, CD16 and NKG2D activate pSLP76 to a greater degree than 2B4, and this difference is accentuated in cluster 2 (p<0.05), where the initial concentration of SLP76 is highest (**Figure S6**). The signal strength of pAkt (**Figure 4F**, *right column*) is comparable across both the clusters and the pathways with no statistically significant differences.

Indeed, the signaling dynamics are quite complex. Nonetheless, some generalizations can be made when the network is collectively considered (**Figure 4**). On average, the signaling time and the signal strength of the species are faster and greater, respectively, under CD16 or NKG2D stimulation compared to 2B4. Contrastingly, the signal duration of the species is, on average, relatively longer under 2B4 stimulation. Taken together, the baseline model predictions reveal qualitative similarities and differences between the pathways. This detailed insight into each pathway is not

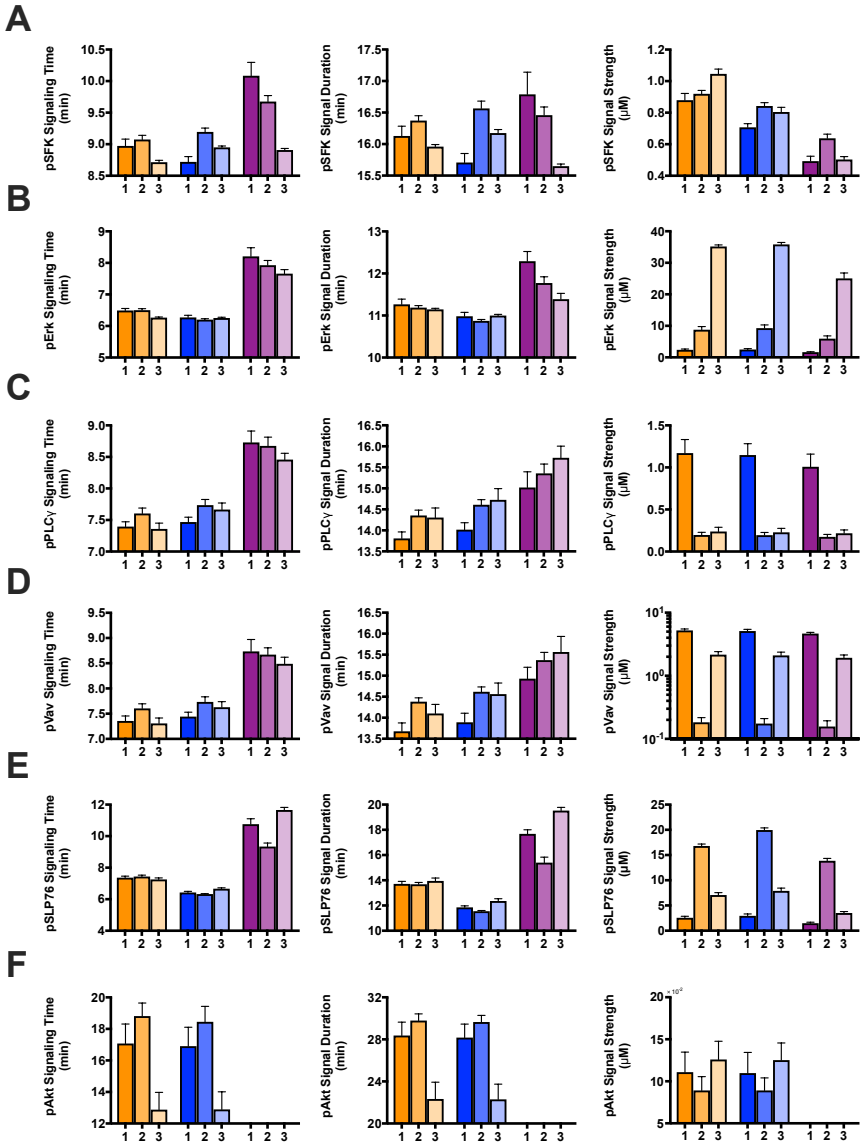

Fig. 4. Baseline model predictions. The signaling time (*left column*), signal duration (*middle column*) and signal strength (*right column*) of pSFK (**A**), pErk (**B**), pPLCγ (**C**), pVav (**D**), pSLP76 (**E**) and pAkt (**F**) are shown. Blue: CD16 pathway. Purple: 2B4 pathway. Orange: NKG2D pathway. Bars: median value of 1000 simulations. Error bars: 95% confidence interval of median. Clusters are shown in the horizontal axes ("1", "2", and "3"). Kruskal-Wallis test was used to determine statistical significance between groups in Prism (GraphPad).

directly apparent by just looking at the experimental measurements.

3.4 Parameter estimates explain baseline model predictions

We analyzed the estimated parameter values to better understand the differences between the pathways (**Figure 5**). We first calculated the affinity (K_D) between the receptors and their ligands (**Figure 5A,** *left*). CD16 has a tighter affinity (smaller K_D) or its ligand when compared to NKG2D and 2B4 (p<0.05) with the following trend in the affinity being observed: CD16 ≫ NKG2D ≫ 2B4. We calculated the catalytic efficiencies for receptor activation and deactivation (**Figure 5A,** *center*), as well as pSFK activation and deactivation (**Figure 5A,** *right*). The efficiency of CD16 and NKG2D activation (**Figure 5A,** *center*) are identical, whereas 2B4 activation is approximately 40% more efficient (p<0.05)The efficiency of receptor deactivation shows a different trend: CD16 > 2B4 > NKG2D. The efficiency of pSFK activation is greatest when NKG2D is stimulated, compared to CD16 or 2B4 (**Figure 5A,** *right*).

Although CD16 binds to its ligand tightly, the efficiency of CD16 deactivation is approximately 60% greater than CD16 activation. This suggests that signal transduction via CD16 starts rapidly and ends quickly. Despite 2B4's weak affinity for its ligand, its efficiency for activation is approximately 40% greater than deactivation. Thus, signaling mediated by 2B4 starts very slow but also turns off slowly. NKG2D's affinity for its ligand is stronger than that of 2B4, but not as strong as CD16. However, its efficiency for activation can be almost twice as much as its efficiency for deacti-

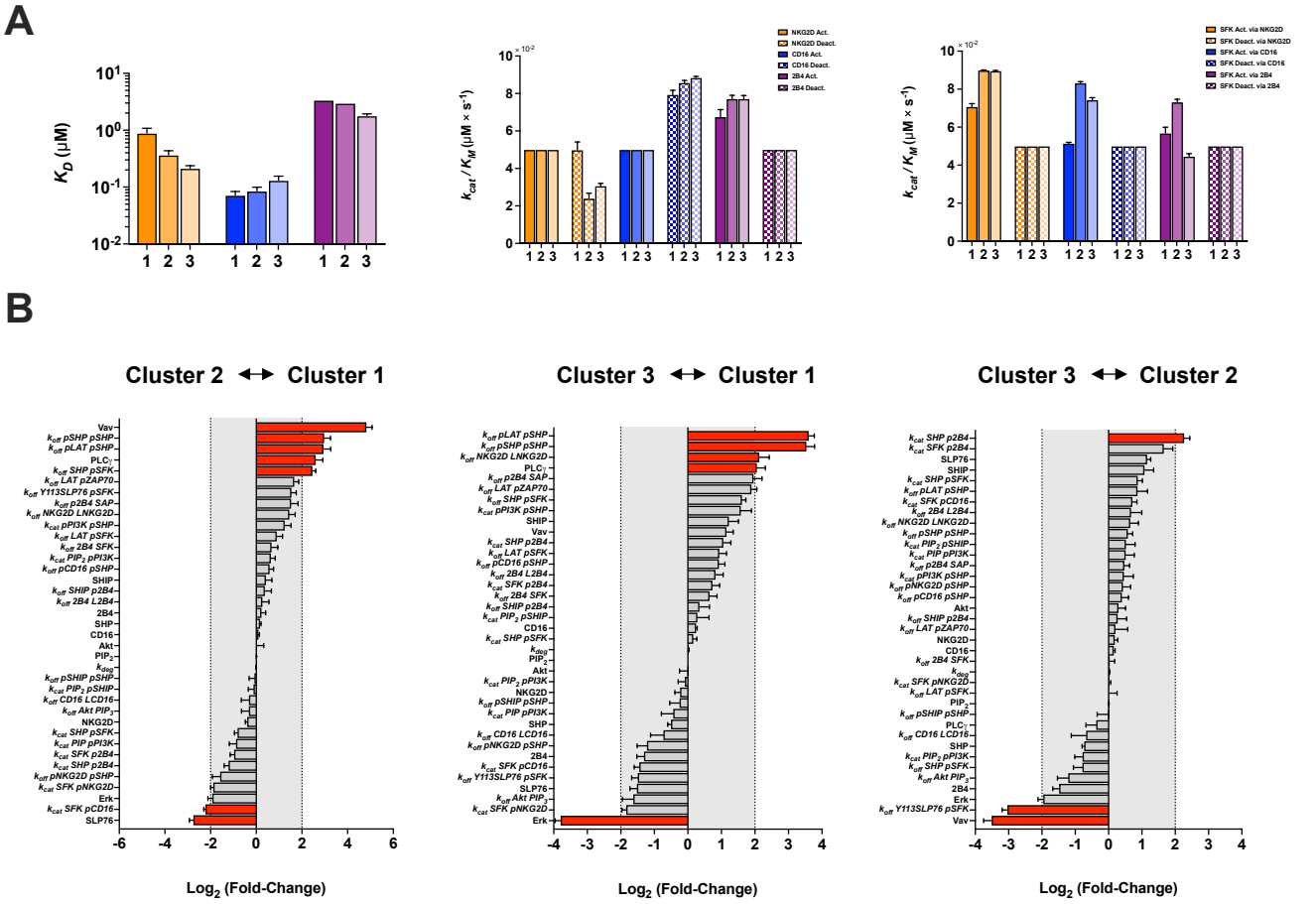

Fig. 5. Analysis of estimated parameters. Receptor-ligand affinities (**A**, *left panel*), catalytic efficiency of receptor activation/deactivation (**A**, *middle panel*) and SFK activation/deactivation (**A**, *right panel*) are shown. Clusters are shown on the horizontal axes. Values without error bars did not contain parameters during initial parameter estimation. Pairwise cluster comparison of estimated parameter values between clusters 1 and 2 (**B**, *left panel*), clusters 1 and 3 (**B**, *middle panel*) and clusters 2 and 3 (**B**, *right panel*). Bars: median value from 1000 simulations. Error bars: 95% confidence interval of median. Kruskal-Wallis test was used to determine statistical significance between groups in Prism (GraphPad).

vation, which suggests signal transduction via NKG2D starts relatively quickly and ends much more slowly.

We quantified the fold-change of each of the estimated parameters in a pairwise fashion between the three clusters (**Figure 5B**) and focused on cases where the $\log_2$ fold-change between two clusters is $\geq |2|$ (shown in red). The bars represent the median fold-change from 1,000 estimates of each cluster and the error bars indicate the 95% confidence interval. This analysis shows that cluster 1 has a greater initial concentration of Vav and PLCγ, higher k_{off} value for pSHP and pLAT deactivation and a higher k_{off} value for pSHP activation deactivation, compared to the cluster 2 (**Figure 5B,** *left*). On the other hand, cluster 2 has a greater concentration of SLP76 and a greater k_{cat} value for pSFK activation via CD16 stimulation. Comparing clusters 1 and 3 shows that cluster 1 has a higher initial concentration of PLCγ, greater k_{off} value for pSHP and pLAT deactivation and a higher k_{off} value between NKG2D and its ligand (**Figure 5B,** *center*). Cluster 3 has a higher initial concentration Erk when compared to cluster 1. Lastly, cluster 2 shows a higher kcat value for pSHP activation via 2B4 stimulation. However, cluster 3 has a much greater initial value for Vav and k_{off} value for SLP76 phosphorylation at site Y113 (**Figure 5B**, *right*).

These comparisons of the estimated kinetic parameters and initial concentrations directly affect the simulated signaling dynamics. For example, the signal strength of pErk (**Figure 4B**, *right column*), pPLCγ (**Figure 4C**, *right column*), pVav (**Figure 4E**, *right column*) and pSLP76 (**Figure 4F**, *right column*) are correlated with their respective initial values; that is, the higher the initial concentration, the greater the signal strength. The signaling time and signal duration of pAkt (**Figure 4F**, *middle* and *right columns*) is much faster and longer, respectively, in cluster 3 even though the estimated concentration of Akt is indistinguishable between the clusters (**Figure 5B**). This is explained by the lower concentration of SHIP in cluster 3, which dephosphorylates PIP_3 (the catalyst of pAkt activation in the present model) into PIP_2. In other words, as the concentration of pSHIP decreases, the rate of pAkt activation increases. Taken together, our analyses of the estimated parameter values provide the mechanistic insight needed to understand the differences in the signaling dynamics across the pathways and the clusters.

3.5 Differential effects of combinatorial stimulations

We next investigated how combinatorial receptor stimulation, using various ligand concentrations, impacts pSFK activation using the same three metrics. The pSFK species is a signaling node activated by all three receptors, and it initiates downstream signaling through each of the PI3K-Akt, SLP76-Vav-Erk, and PLCγ pathways. Thus, studying pSFK is a way to understand how the inputs from different receptor ligands are integrated to promote the activation of signaling species that mediate NK cell activation. Here, we varied the ligand concentrations from baseline (66.7 nM) up to a ten-fold increase (667 nM). Since there are three pathways in the present model, there are three different combinations of co-stimulation: (1) 2B4 + NKG2D, (2) CD16 + 2B4 and (3) CD16 + NKG2D. For each of the possible combinations of dual stimulation, we show how the median value from 1,000 simulations changes as the concentration of ligands changes. Generally, the qualitative trends and results of our analysis of **Figure 6** translate well across the remaining clusters.

In general, as more ligands are introduced into the system, the signaling time (**Figure 6A**) and signal duration (**Figure 6B**) decrease, while the signal strength (**Figure 6C**) increases. This intuitively makes sense, as greater stimulation of multiple pathways should lead to faster and stronger signaling. Unexpectedly, the model predicts a biphasic response that is most pronounced when 2B4 is stimulated (**Figure 6**, *left* and *middle columns*). This novel prediction suggests there exists optimal ligand concentrations that enhance cell signaling such that signaling time is fast but signal duration and strength are large (for example, ~300 nM of NKG2D and 2B4 ligands each; **Figure 6**, *left column*). Overall, increasing either the CD16 or NKG2D ligands decreases the signaling time while increasing the signal strength of pSFK. Also, having more 2B4 ligands mostly increases the signal duration of pSFK until the ligand concentration reaches approximately 300 nM. Taken together, the model predictions suggest that optimal activation of pSFK is uniquely determined by the stimulation of NKG2D and 2B4. Since these pathways induce qualitatively different effects on the signaling network, our simulated results indicate the importance of activating pathways with dissimilar modes of cell stimulation.

In summary, upon combinatorial receptor stimulation, the time required for species activation and the time interval of species activation decrease, while the magnitude of species activation increases.

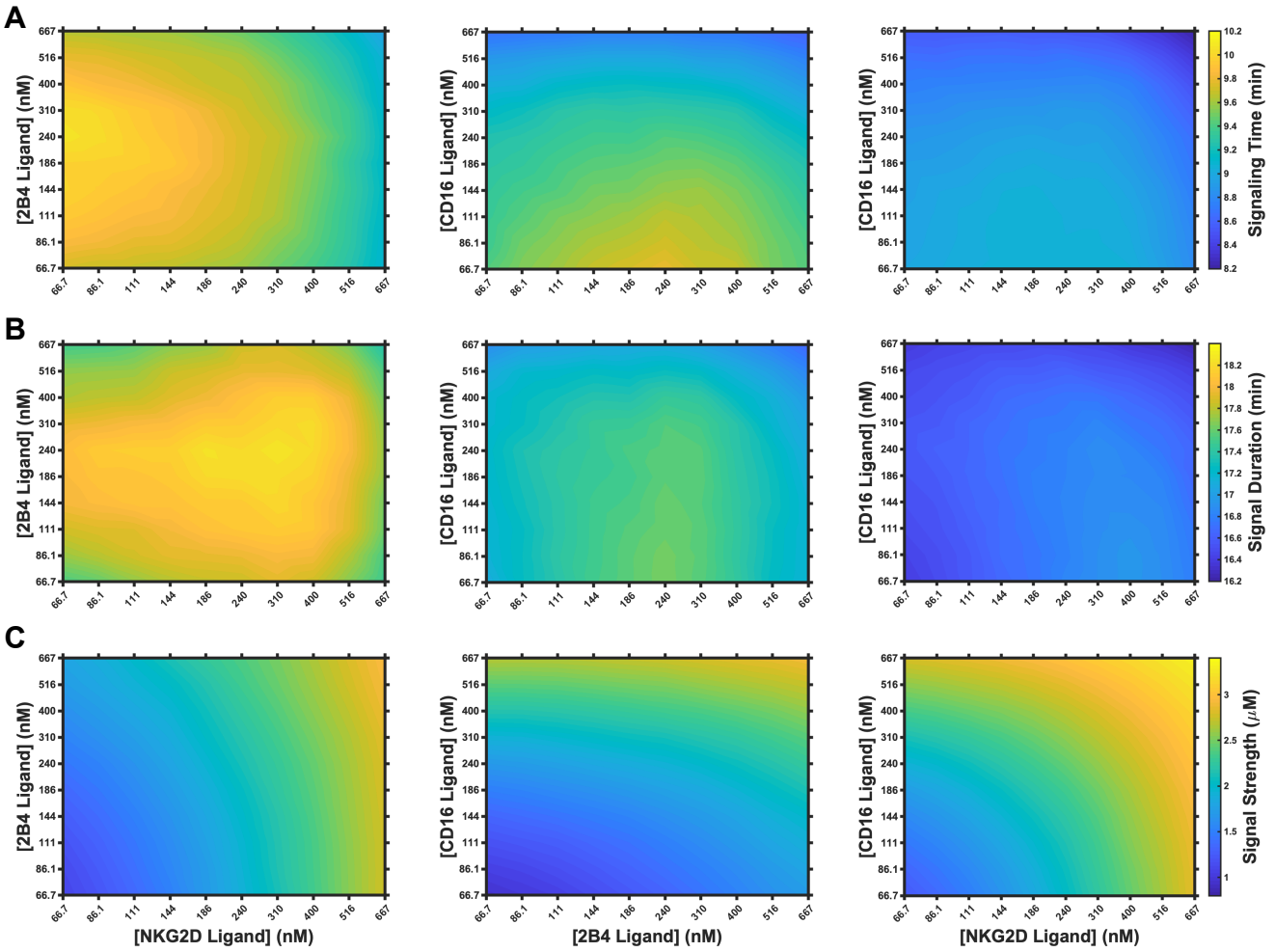

Fig. 6. Effects of combinatorial receptor stimulation. The signaling time (**A**), signal duration (**B**) and signal strength (**C**) of pSFK from cluster 1 under co-stimulation of 2B4 and NKG2D (*left column*), CD16 and 2B4 (*middle column*), and CD16 and NKG2D (*right column*).

3.6 Perturbation of the stimulatory network

Phosphorylated SFK and the activated phosphatases (pSHP and pSHIP) play opposing roles during signal transduction. We varied four sets of parameters that regulate the activity of these species to determine how they impact the signaling dynamics (**Figure S8**). We simulated the perturbations by varying the koff values to different degrees, which affects the catalytic efficiency of the reactions. Here, we present the results from cluster 1, which holds true for the remaining clusters.

One goal of the perturbations was to reduce the signal-

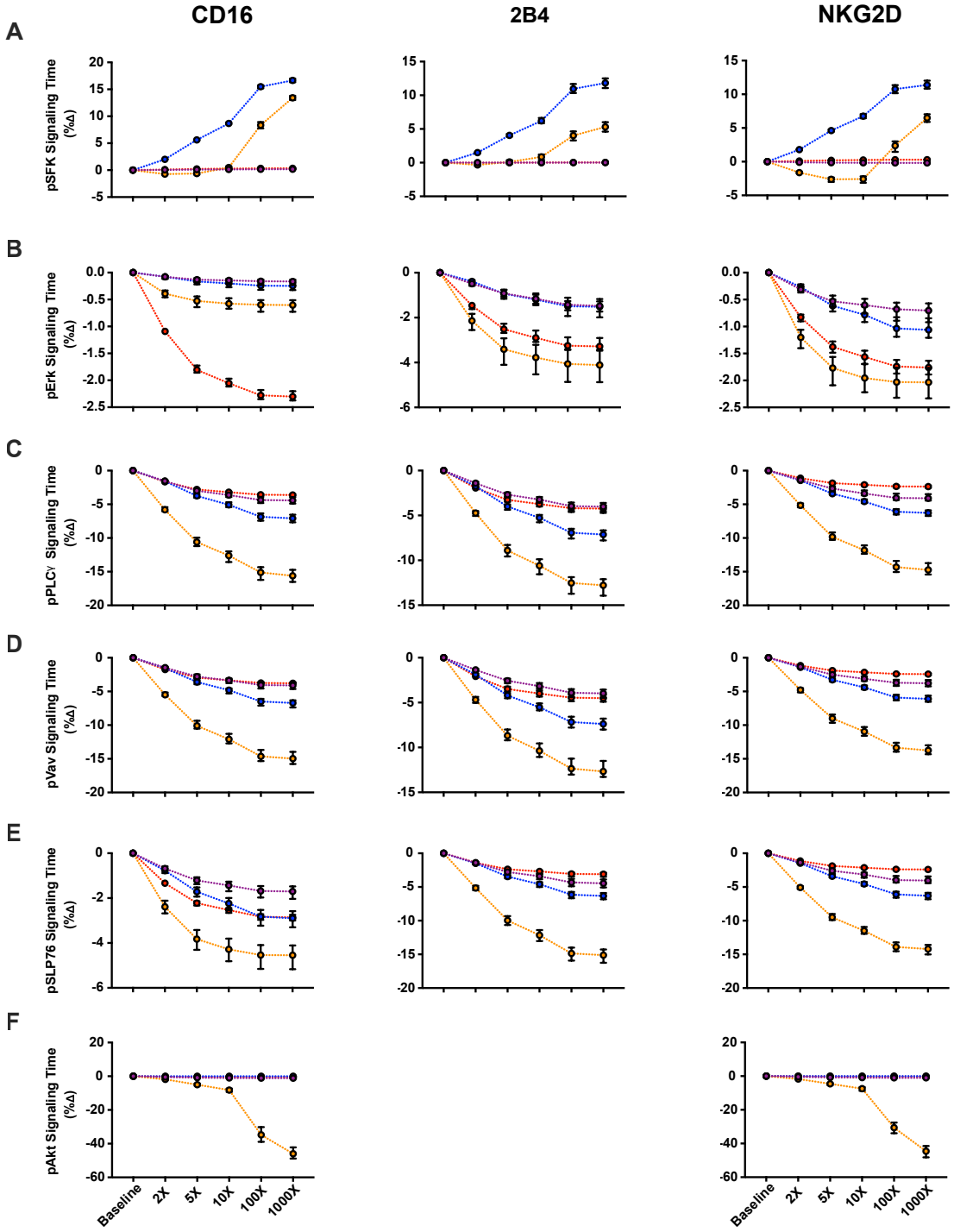

Fig. 7. Differential effects of various perturbations on the signaling time of the species. The percent change of pSFK (**A**), pErk (**B**), pPLCγ (**C**), pVav (**D**), pSLP76 (**E**) and pAkt (**F**) under CD16 (*left column*), 2B4 (*middle column*) or NKG2D (*right column*) stimulation are shown. Red: increasing pSFK activation rate. Blue: decreasing pSFK deactivation rate. Orange: decreasing phosphatase activation rate. Purple: increasing phosphatase deactivation rate. Circles: median value from 1000 simulations. Error bars: 95% confidence interval of median. Kruskal-Wallis test was used to determine statistical significance between groups in Prism (GraphPad).

ing time, which is analogous to faster signaling (**Figure 7**). In general, the model predicts that decreasing the activation rate of the phosphatases decreases the signaling time the most (**Figure 7B-F**, *orange curves*), compared to the other perturbations ($p<0.05$). There are two exceptions. For pSFK, the four perturbations either increase pSFK signaling time or have no effect (**Figure 7A**). Additionally, for pErk, increasing the pSFK activation is most effective in reducing the signaling time upon stimulation with CD16 (**Figure 7B**, *left column*, red curve). Another goal was to increase the signal duration, which is analogous to longer signaling (**Figure S9**). Surprisingly, none of the perturbations increased the signal duration of the species. Instead, signal duration decreased as the perturbations increased in magnitude, where the largest decrease was observed when activation of the phosphatases was inhibited ($p<0.05$). Increasing the signal strength was another goal, which is analogous to activating more species (**Figure 8**). Overall, the signal strength of the species (**Figure 8B-F**, *orange curve*) is more sensitive to changes in the activation rate of the phosphatases ($p<0.05$). Phosphorylated SFK is again an exception here, where both decreasing the activation rate of the phosphatase (**Figure 8A**, *orange curve*) and decreasing pSFK deactivation rate (**Figure 8A**, *blue curve*) significantly increase its signal strength.

In summary, the model predicts that the phosphatases strongly regulate the activation of the stimulatory network, and that inhibiting their activation leads to faster signaling and increases the amount of activated species. This leads to a sharper, more pulsatile response of the species' concentration (**Figure S10**) by disinhibiting the flow of signal transduction (**Figure S11**). Our simulations provide quantitative insight into mechanisms that can augment the activation of the stimulatory network in NK cells.

DISCUSSION

In the present study, we constructed a mathematical model of a subset of the signaling pathways that mediate NK cell activation. We applied the model to understand the differences between the different stimulatory pathways, how these pathways influence NK cell activation and how downstream species activation can be enhanced via perturbations. Although NK cell stimulation has been previously modeled, those works do not address these questions. Our baseline model predictions demonstrate that, on average, CD16 and NKG2D activate the species more rapidly and to a greater degree than 2B4; contrastingly, 2B4 activates the signaling species over a longer time interval. Analyses of the model's estimated parameters help explain these predictions. The parameter values show that CD16's activation is fast, and its deactivation is even faster. The activation of 2B4 is estimated to be the slowest of the three pathways, but its deactivation rate is even slower. NKG2D, on the other hand, is activated faster than 2B4, while its deactivation rate is slower than CD16's. This suggests NKG2D's activation profile is the optimum compared to the other pathways. The *in silico* studies of receptor co-stimulation suggest optimal activation is achieved via 2B4 and NKG2D stimulation. In addition, the *in silico* perturbations reveal that the rate and magnitude of species activation are particularly sensitive to inhibiting the activation of the phosphatases. Our computational modeling is highly valuable, as the above studies may require a large amount of time to complete through experimentation alone.

Some researchers have concluded that CD16 plays the dominant role in NK cell activation, compared to other receptor signaling pathways (20,44,45). However, the lack of quantification of the receptors and the signaling species in such studies makes it difficult to deduce which pathway is more influential in cell activation. In calibrating our model to experimental data, we find that the average amount of activated species (i.e., signal strength) is highly dependent on the initial concentrations of the stimulatory receptors and intracellular signaling species (**Figures 4-5**). Using the calibrated and validated model, we predict that no individual pathway is dominant in activating the signaling species. The results of the current study, overall, challenge the notion of a single dominant pathway in NK cell activation. Instead, the model shows that co-stimulation is an effective means of producing stronger activation. Additionally, NK cells have evolved to express an abundance of stimulatory receptors, unlike T and B cells, which further supports the importance of co-stimulation as an optimal method of NK cell activation.

Researchers in recent years have designed chimeric antigen receptors (CARs) for NK cells that include intracellular signaling domains of CD16, 2B4 and NKG2D for anti-tumor therapy (46,47). It is not unexpected that CARs comprised of CD16, 2B4 and NKG2D signaling domains together outperformed activation of the individual receptors, as supported by our model. Indeed, CAR-NK cell immunotherapies (48,49) that include intracellular domains from both CD16 and NKG2D are shown to be effective in eliminating tumors in pre-clinical studies. Through continued success in the pre-clinical stage, a few CAR-NK cell immunotherapies have entered clinical trials as potential therapeutics for cancer patients (2,50). In total, the analyses carried out in this paper provide additional support for the stimulation of multiple pathways as the more effective method of NK cell activation. Our model predictions also give mechanistic insight into why the combinations are superior.

We acknowledge some limitations that may affect the model predictions. Firstly, our model includes three important stimulatory receptors. Several others could be considered; however, this work provides a novel foundation with which to study signal transduction and integration with more than one receptor. Additionally, although multiple sites of phosphorylation and dephosphorylation can exist for each species, we have not included this level of detail in the model. This would increase the specificity of our model, but it would be at the expense of model simplicity. Since we are interested in understanding and comparing the dynamics between multiple pathways, we sought to simplify the pathways in order to effectively compare them. In the future, researchers can adopt and improve the current model by considering site specific reactions and their importance in particular aspects of NK cell activation. Finally, although the initial conditions and parameters were derived from literature when available (26–29), we expect that these values may differ based on the specific NK cell line or the donor for primary NK cells.

Future research can address these limitations, building upon the work presented here.

Despite these limitations, our mathematical model is relevant for understanding NK cell activation and guiding the development of NK cell-based therapies. The results presented here can aid in the design of engineered receptors, such as CARs, by predicting which combinations of signaling domains activate NK cells and induce optimal killing of target cells. Questions within tumor immunology, in particular tumor and NK cell dynamics, can be studied by integrating the pre-

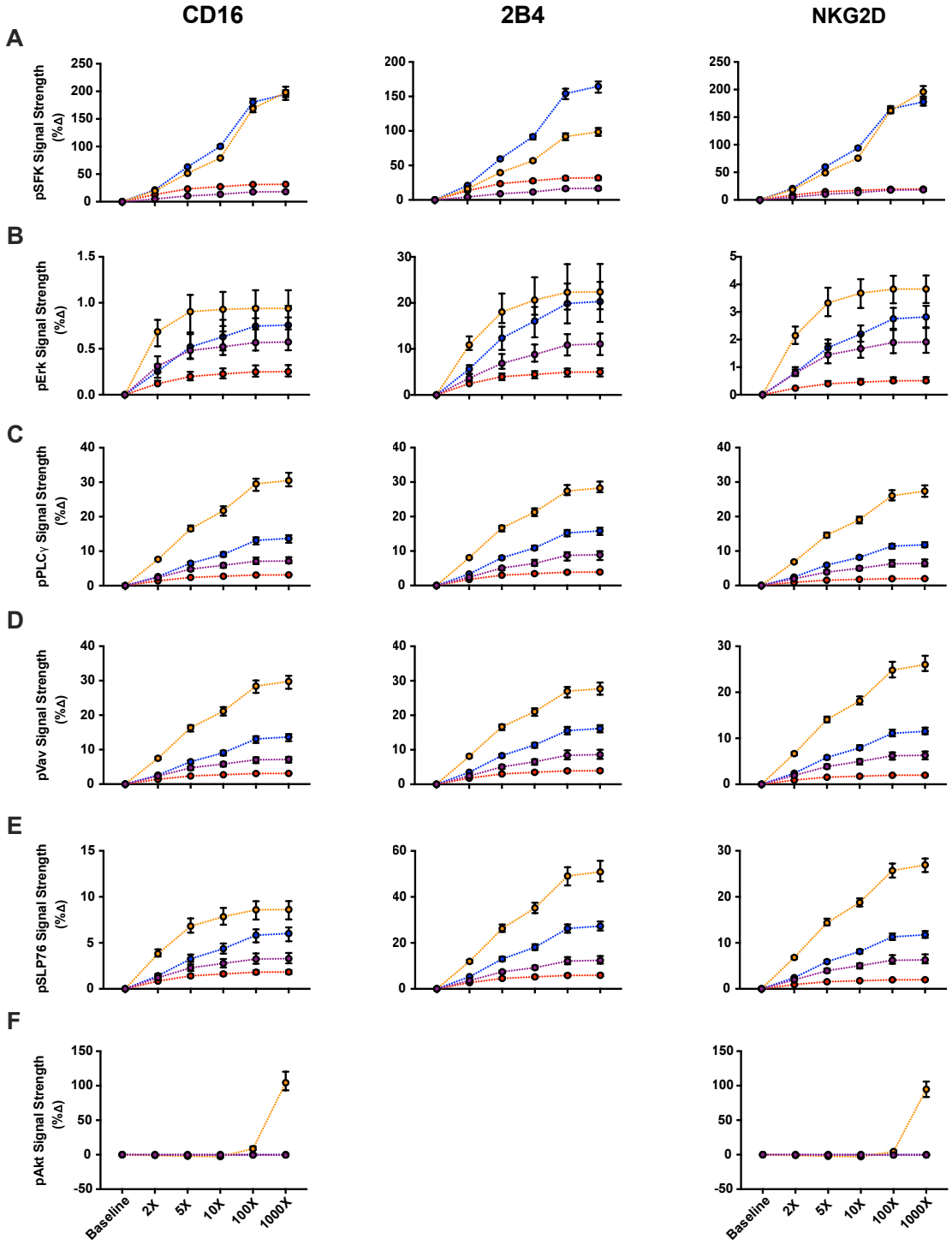

Fig. 8. Differential effects of various perturbations on the signaling time of the species. The percent change of pSFK (**A**), pErk (**B**), pPLCγ (**C**), pVav (**D**), pSLP76 (**E**) and pAkt (**F**) under CD16 (*left column*), 2B4 (*middle column*) or NKG2D (*right column*) stimulation are shown. Red: increasing pSFK activation rate. Blue: decreasing pSFK deactivation rate. Orange: decreasing phosphatase activation rate. Purple: increasing phosphatase deactivation rate. Circles: median value from 1000 simulations. Error bars: 95% confidence interval of median. Kruskal-Wallis test was used to determine statistical significance between groups in Prism (GraphPad).

sent signaling model with a cell-based model, for example work by Mahasa and coworkers (13). Furthermore, incorporating inhibitory pathways could help explain how tumor cells escape NK cell cytotoxicity by engaging with NK cell inhibitory receptors. In conclusion, our work delineates the differences between multiple stimulatory pathways involved in NK cell activation, and the model presented here can be utilized as a framework for researchers interested in NK cell-mediated cytotoxicity and its applications in immunotherapy.

ACKNOWLEDGEMENTS

We immensely appreciate the Finley research group for critical evaluation of this manuscript as well as improvements to the model code. This work was supported a Viterbi/Graduate School Merit Fellowship (to S.Z.M).

SUPPORTING INFORMATION

File S1. Computational model as MATLAB (.m) and BioNetGen (.bngl) files

File S2. MATLAB data file (.mat) containing the list of species' names and parameter labels, and species' initial concentrations and parameter values for each cluster

File S3. Supplemental tables with the list of model species, reactions and parameters

File S4. Supplemental figures

REFERENCES

1. Baxter AG, Hodgkin PD. Activation rules: the two-signal theories of immune activation. Nat Rev Immunol. 2002 Jun;2(6):439–46.
2. Bollino D, Webb TJ. Chimeric antigen receptor–engineered natural killer and natural killer T cells for cancer immunotherapy. Transl Res. 2017 Sep;187:32–43.
3. Klingemann H-G. Natural killer cell-based immunotherapeutic strategies. Cytotherapy. 2005 Mar;7(1):16–22.
4. Gattinoni L, Jr DJP, Rosenberg SA, Restifo NP. Adoptive immunotherapy for cancer: building on success. Nat Rev Immunol. 2006 May;6(5):383–93.
5. Rosenberg SA, Yang JC, Restifo NP. Cancer immunotherapy: moving beyond current vaccines. Nat Med. 2004 Sep;10(9):909–15.
6. Mellman I, Coukos G, Dranoff G. Cancer immunotherapy comes of age. Nature. 2011 Dec;480(7378):480–9.
7. Bryceson YT, Ljunggren H-G. Natural Killer Cells: Biology, Physiology and Medicine – Part 1. J Innate Immun. 2011;3(3):213–5.
8. Bryceson YT, Ljunggren H-G. Natural Killer Cells: Biology, Physiology and Medicine – Part 2. J Innate Immun. 2011;3(4):327–8.
9. Guillerey C, Huntington ND, Smyth MJ. Targeting natural killer cells in cancer immunotherapy. Nat Immunol. 2016 Sep;17(9):1025–36.
10. Das J. Activation or Tolerance of Natural Killer Cells Is Modulated by Ligand Quality in a Nonmonotonic Manner. Biophys J. 2010 Oct;99(7):2028–37.
11. Mesecke S, Urlaub D, Busch H, Eils R, Watzl C. Integration of Activating and Inhibitory Receptor Signaling by Regulated Phosphorylation of Vav1 in Immune Cells. Sci Signal. 2011 May 31;4(175):ra36–ra36.
12. Pappalardo F, Palladini A, Pennisi M, Castiglione F, Motta S. Mathematical and Computational Models in Tumor Immunology. Math Model Nat Phenom. 2012;7(3):186–203.
13. Mahasa KJ, Ouifki R, Eladdadi A, Pillis L de. Mathematical model of tumor–immune surveillance. J Theor Biol. 2016 Sep;404:312–30.
14. Hoffman F, Gavaghan D, Osborne J, Barrett IP, You T, Ghadially H, et al. A mathematical model of antibody-dependent cellular cytotoxicity (ADCC). J Theor Biol. 2018 Jan;436:39–50.
15. Scherbakova A, Lust H, Everaus H, Aints A. A mathematical model of natural killer cell activity. Cytometry A. 2013 Jun;83A(6):585–91.
16. Sternberg-Simon M, Mehr R. Modeling natural killer cell repertoire development and activation dynamics. In World Scientific; 2013 [cited 2018 Jun 25]. p. 132–47. Available from: http://www.worldscientific.com/doi/abs/10.1142/9789814520829_0008
17. Theorell J, Gustavsson A-L, Tesi B, Sigmundsson K, Ljunggren H-G, Lundbäck T, et al. Immunomodulatory activity of commonly used drugs on Fc-receptor-mediated human natural killer cell activation. Cancer Immunol Immunother. 2014 Jun;63(6):627–41.
18. Chen R, Relouzat F, Roncagalli R, Aoukaty A, Tan R, Latour S, et al. Molecular Dissection of 2B4 Signaling: Implications for Signal Transduction by SLAM-Related Receptors. Mol Cell Biol. 2004 Jun 15;24(12):5144–56.
19. Gilfillan S, Ho EL, Cella M, Yokoyama WM, Colonna M. NKG2D recruits two distinct adapters to trigger NK cell activation and costimulation. Nat Immunol. 2002 Dec;3(12):1150–5.
20. Long EO, Sik Kim H, Liu D, Peterson ME, Rajagopalan S. Controlling Natural Killer Cell Responses: Integration of Signals for Activation and Inhibition. Annu Rev Immunol. 2013 Mar 21;31(1):227–58.
21. Kim HS, Long EO. Complementary Phosphorylation Sites in the Adaptor Protein SLP-76 Promote Synergistic Activation of Natural Killer Cells. Sci Signal. 2012 Jul 10;5(232):ra49–ra49.
22. Kwon H-J, Kim HS. Signaling for Synergistic Activation of Natural Killer Cells. Immune Netw. 2012;12(6):240.
23. Harris LA, Hogg JS, Tapia J-J, Sekar JAP, Gupta S, Korsunsky I, et al. BioNetGen 2.2: advances in rule-based modeling. Bioinformatics. 2016 Nov 1;32(21):3366–8.
24. Kim HS, Das A, Gross CC, Bryceson YT, Long EO. Synergistic Signals for Natural Cytotoxicity Are Required to Overcome Inhibition by c-Cbl Ubiquitin Ligase. Immunity. 2010 Feb;32(2):175–86.
25. Szewczuk LM, Tarrant MK, Cole PA. Protein Phosphorylation by Semisynthesis: From Paper to Practice. Methods Enzymol. 2009;462:1–24.
26. Northrup SH, Erickson HP. Kinetics of protein-protein association explained by Brownian dynamics computer simulation. Proc Natl Acad Sci. 1992 Apr 15;89(8):3338–42.
27. Schlosshauer M, Baker D. Realistic protein–protein association rates from a simple diffusional model neglecting long-range interactions, free energy barriers, and landscape ruggedness. Protein Sci. 13(6):1660–9.
28. Kim M-S, Pinto SM, Getnet D, Nirujogi RS, Manda SS, Chaerkady R, et al. A draft map of the human proteome. Nature. 2014 May;509(7502):575–81.
29. Bar-Even A, Noor E, Savir Y, Liebermeister W, Davidi D, Tawfik DS, et al. The Moderately Efficient Enzyme: Evolutionary and Physicochemical Trends Shaping Enzyme Parameters. Biochemistry. 2011 May 31;50(21):4402–10.
30. Billadeau DD, Upshaw JL, Schoon RA, Dick CJ, Leibson PJ. NKG2D-DAP10 triggers human NK cell–mediated killing via a Syk-independent regulatory pathway. Nat Immunol. 2003 Jun;4(6):557–64.
31. Dong Z, Davidson D, Pérez-Quintero LA, Kurosaki T, Swat W, Veillette A. The Adaptor SAP Controls NK Cell Activation by Regulating the Enzymes Vav-1 and SHIP-1 and by Enhancing Conjugates with Target Cells. Immunity. 2012 Jun;36(6):974–85.
32. Ting AT, Karnitz LM, Schoon RA. Fc7 Receptor Activation Induces the Tyrosine Phosphorylation of Both Phospholipase C (PLC)-y1 and PLC-y2 in Natural Killer Cells. 1992;5.
33. Marino S, Hogue IB, Ray CJ, Kirschner DE. A Methodology For Performing Global Uncertainty And Sensitivity Analysis In Systems Biology. J Theor Biol. 2008 Sep 7;254(1):178–96.
34. Kennedy J. Particle Swarm Optimization. In: Encyclopedia of Machine Learning [Internet]. Springer, Boston, MA; 2011 [cited 2018 Jun 25]. p. 760–6. Available from: https://link.springer.com/referenceworkentry/10.1007/978-0-387-30164-8_630
35. Tikhonov AN. Numerical methods for the solution of ill-posed problems. Dordrecht; London: Springer; 2011.
36. Heinrich R, Neel BG, Rapoport TA. Mathematical Models of Protein Kinase Signal Transduction. Mol Cell. 2002 May;9(5):957–70.
37. Pérez-Quintero L-A, Roncagalli R, Guo H, Latour S, Davidson D, Veillette A. EAT-2, a SAP-like adaptor, controls NK cell activation through phospholipase Cγ, Ca++, and Erk, leading to granule polarization. J Exp Med. 2014 Apr 7;211(4):727–42.

38. Kwon H-J, Kwon SJ, Lee H, Park H-R, Choi G-E, Kang S-W, et al. NK cell function triggered by multiple activating receptors is negatively regulated by glycogen synthase kinase-3β. Cell Signal. 2015 Sep;27(9):1731–41.
39. Kwon H-J, Choi G-E, Ryu S, Kwon SJ, Kim SC, Booth C, et al. Stepwise phosphorylation of p65 promotes NF-κB activation and NK cell responses during target cell recognition. Nat Commun. 2016 May 25;7:11686.
40. Arthur D, Vassilvitskii S. k-means++: The Advantages of Careful Seeding. :11.
41. Principal Component Analysis | I.T. Jolliffe | Springer [Internet]. [cited 2018 Jun 25]. Available from: https://www.springer.com/us/book/9780387954424
42. Efron B. Bootstrap Methods: Another Look at the Jackknife. Ann Stat. 1979;7(1,):1–26.
43. Dixon PM. Bootstrap Resampling. In: El-Shaarawi AH, Piegorsch WW, editors. Encyclopedia of Environmetrics [Internet]. Chichester, UK: John Wiley & Sons, Ltd; 2006 [cited 2018 Dec 28]. Available from: http://doi.wiley.com/10.1002/9780470057339.vab028
44. Bhat R, Watzl C. Serial Killing of Tumor Cells by Human Natural Killer Cells – Enhancement by Therapeutic Antibodies. Zimmer J, editor. PLoS ONE. 2007 Mar 28;2(3):e326.
45. Romain G, Senyukov V, Rey-Villamizar N, Merouane A, Kelton W, Liadi I, et al. Antibody Fc engineering improves frequency and promotes kinetic boosting of serial killing mediated by NK cells. Blood. 2014 Nov 20;124(22):3241–9.
46. Altvater B, Landmeier S, Pscherer S, Temme J, Schweer K, Kailayangiri S, et al. 2B4 (CD244) Signaling by Recombinant Antigen-specific Chimeric Receptors Costimulates Natural Killer Cell Activation to Leukemia and Neuroblastoma Cells. Clin Cancer Res. 2009 Aug 1;15(15):4857–66.
47. Li Y, Hermanson DL, Moriarity BS, Kaufman DS. Human iPSC-Derived Natural Killer Cells Engineered with Chimeric Antigen Receptors Enhance Anti-tumor Activity. Cell Stem Cell [Internet]. 2018 Jun [cited 2018 Aug 1]; Available from: https://linkinghub.elsevier.com/retrieve/pii/S1934590918302844
48. Glienke W, Esser R, Priesner C, Suerth JD, Schambach A, Wels WS, et al. Advantages and applications of CAR-expressing natural killer cells. Front Pharmacol [Internet]. 2015 Feb 12 [cited 2018 Jun 25];6. Available from: http://journal.frontiersin.org/Article/10.3389/fphar.2015.00021/abstract
49. Romanski A, Uherek C, Bug G, Seifried E, Klingemann H, Wels WS, et al. CD19-CAR engineered NK-92 cells are sufficient to overcome NK cell resistance in B-cell malignancies. J Cell Mol Med. 2016 Jul;20(7):1287–94.
50. Tang X, Yang L, Li Z, Nalin AP, Dai H, Xu T, et al. First-in-man clinical trial of CAR NK-92 cells: safety test of CD33-CAR NK-92 cells in patients with relapsed and refractory acute myeloid leukemia. Am J Cancer Res. 2018 Jun 1;8(6):1083–9.